Navier-Stokes Computation of Flow Around a Round-Edged Double-Delta Wing

C.-H. Hsu*
Vigyan, Inc., Hampton, Virginia
and
C. H. Liu†
NASA Langley Research Center, Hampton, Virginia

Computations of three-dimensonal vortical flows over a thin round-edged double-delta wing with an aspect ratio of 2.05 are performed using an implicit upwind-relaxation finite-difference scheme. The effects of grid and angle of attack on the Navier-Stokes computations are studied. Coarse-grid calculations cannot predict the detailed structures of the vortical flowfields for lack of grid resolution. On the contrary, fine-grid computations show that key features of vortex formation, interaction, and breakdown are simulated. Furthermore, computed lift coefficients and spanwise surface static pressure distributions are in good agreement with the experimental data up to $\alpha = 25°$.

Nomenclature

A, B, C	= Jacobian matrices of E, F, G
AR	= aspect ratio
C	= wing root chord = 1
CFL	= Courant number
C_L	= wing lift coefficient = lift/qS
C_p	= static pressure coefficient = $2p$
C_t	= total pressure coefficient = $2p + u^2 + v^2 + w^2$
E, F, G	= inviscid flux vectors of conservation equations
E_V, F_V, G_V	= viscous flux vectors of conservation equations
I	= identity matrix
J	= Jacobian of coordinate transformation
L_2	= L_2 norm of all residuals
P	= static pressure
p	= normalized static pressure = $(P - P_\infty)/2q$
Q	= dependent variable = $Q(p, u, v, w)$
q	= dynamic pressure = $\rho V_\infty^2/2$
R^*, S^*, T^*	= linearized coefficient matrices of E_V, F_V, G_V
Re	= Reynolds number = $\rho V_\infty C/\mu$
S	= wing planform area; also local semispan
t	= time
u, v, w	= velocity components in the Cartesian frame
V	= magnitude of flow velocity
X, Y, Z	= Cartesian coordinates
x, y, z	= normalized Cartesian coordinates
α	= angle of attack
β	= pseudocompressibility parameter
ζ, ξ, η	= curvilinear coordinates
μ	= molecular viscosity = constant
ρ	= density = constant

Subscripts

C	= Cartesian frame
V	= viscous shear stress
∞	= freestream condition

Superscripts

n	= time level of previous step
T	= transpose of

Introduction

THE rapid advancement of flight vehicle technology has resulted in a substantial increase in the complexity of aerodynamic designs and corresponding flowfields. For example, modern combat airplanes and tactical missiles are often designed to fly at high angles of attack to achieve supermaneuverability and agility. Flowfields around these high-performance aircraft are characterized by large regions of three-dimensional separated and vortical flows. To investigate those complicated fluid mechanisms and subsequently develop flow control concepts, a lot of experiments have been made in water facilities and low-speed wind tunnels.

Typical wing geometries of advanced fighter aircraft are thin and highly-swept strake-wings with relatively sharp leading edges. Strake wings or wings with kinked leading-edges such as double-delta wings are characterized by separation-induced leeward vortices. The vortices originating from the highly-swept strake can stabilize the leading-edge vortices emanating from the main wing. These concentrated leading-edge vortices generate very low pressure levels on the wing surface directly below the vortical cores, and, hence, result in a large normal force. However, above a crucial angle of attack, the vortices are no longer well-organized or stable. Instead, vortical cores may swell or spiral. This disruption process is termed a vortex breakdown, which may cause performance, control, and stability problems.

In recent years several experimental investigations on double-delta wings have been carried out.[1-5] A typical sketch of experimental flow pattern is shown in Fig. 1. At low angles of attack, two primary vortices, originating from the strake and wing leading edges, are shed leeward on each side of the wing and remain distinguishable over the entire wing. At medium angles of attack, the vortices intertwine about each other and merge into one stable vortex over the rear part of the wing. At

Received May 10, 1988; revision received Jan. 12, 1989.

*Research Scientist. Senior Member AIAA.
†Senior Research Scientist, Fluid Mechanics Division. Senior Member AIAA.

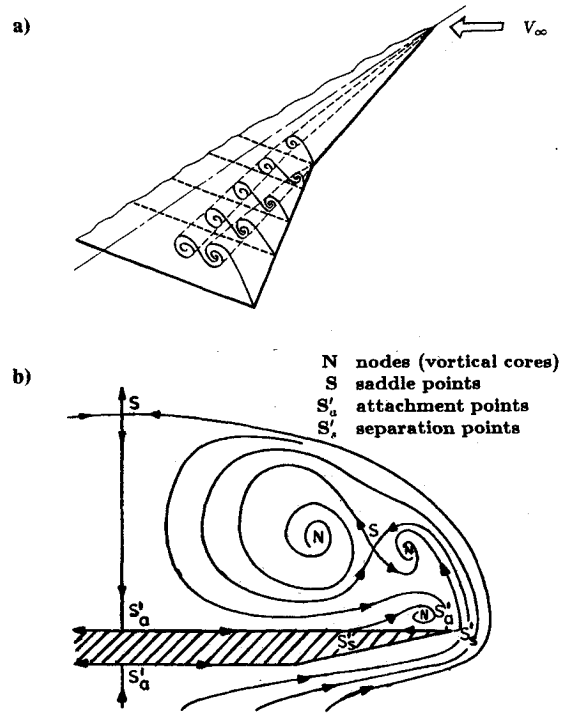

Fig. 1 Experimental observations: a) global vortical pattern, b) crossflow streamline pattern (Verhaagen's sketch) downstream of the kink station.

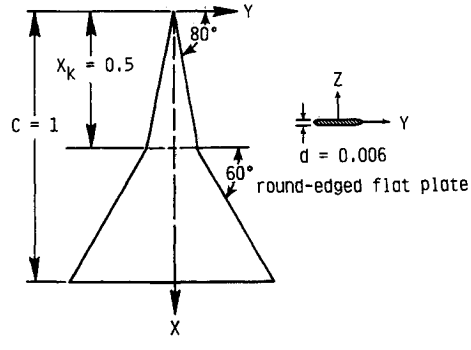

Fig. 2 Test-wing geometry ($AR = 2.05$).

high angles of attack, the vortices merge right after the kink and are no longer separate. At very high angles of attack, the large-scale vortex breakdown inevitably occurs over the wing.

The increased level of confidence attained by a direct simulation of vortex-dominated flows[6-8] has led to more applications of Navier-Stokes solvers to aerodynamic configurations. Recently, several numerical simulations of leading-edge vortices for double-delta wings at low speeds, using different Navier-Stokes solvers, have been reported.[9-11] In the present study, the complex vortical flowfield over a round-edged double-delta wing[1] (Fig. 2) is numerically simulated by solving the incompressible Navier-Stokes equations via an upwind-relaxation finite-difference scheme.[10-13] The main thrust is directed at examining the effects of angle of attack and grid refinement on flowfield computations.

Governing Equations

The governing equations considered here are the three-dimensional, unsteady, incompressible Navier-Stokes equations. These conservation equations of mass and momentum are referred to a body-fitted curvilinear coordinate (ζ, ξ, η) system. By adding an artificial time derivative of the pressure, p_t, to the continuity equation, the conservation equations in the flux vector $(\boldsymbol{E},\boldsymbol{F},\boldsymbol{G})$ form can be formulated as

$$[Q/J]_t + [E - E_V]_\zeta + [F - F_V]_\xi + [G - G_V]_\eta = 0 \qquad (1)$$

with

$$\begin{bmatrix} E - E_V \\ F - F_V \\ G - G_V \end{bmatrix} = \begin{bmatrix} \zeta_x/J & \zeta_y/J & \zeta_z/J \\ \xi_x/J & \xi_y/J & \xi_z/J \\ \eta_x/J & \eta_y/J & \eta_z/J \end{bmatrix} \begin{bmatrix} [E - E_V]_C \\ [F - F_V]_C \\ [G - G_V]_C \end{bmatrix}$$

where

$$Q = [p, u, v, w]^T$$

$$J = det[\partial(\zeta, \xi, \eta)/\partial(x, y, z)]$$

$$E_C = [\beta u, u^2 + p, uv, uw]^T$$

$$F_C = [\beta v, uv, v^2 + p, vw]^T$$

$$G_C = [\beta w, uw, vw, w^2 + p]^T$$

and

$$E_{V,C} = Re^{-1}[0,\ 2u_x,\ u_y + v_x,\ u_z + w_x]^T$$

$$F_{V,C} = Re^{-1}[0,\ v_x + u_y,\ 2v_y,\ v_z + w_y]^T$$

$$G_{V,C} = Re^{-1}[0,\ w_x + u_z,\ w_y + v_z,\ 2w_z]^T$$

The preceding equations are written in a dimensionless form. The flow is assumed laminar and the viscosity is constant. The Cartesian coordinates x, y, and z are nondimensionalized with C. The Cartesian velocities u, v, and w are normalized with the freestream speed, V_∞. The time t is nondimensionalized with C/V_∞ and the normalized pressure is defined as $p = (P - P_\infty)/\rho V_\infty^2$.

The artificial time derivative of the pressure couples the continuity equation with the momentum equations so that the unsteady, incompressible Navier-Stokes equations can be integrated like a conventional parabolic time-dependent system of equations. The parameter β is a measure of the amount of artificial compressibility. For very large β, the modified governing equations recover the Navier-Stokes equations for truly incompressible flow. However, as $\beta \to \infty$ the governing equations become very stiff. On the other hand, if β is chosen to be to small, the upstream influence of a local pressure disturbance is nearly lost, i.e., the system of equations becomes subsonically incompatible. For steady-state calculations, numerical solutions were found[10-13] to converge fast by setting β to unity. When a steady state is approached ($p_t \to 0$) the effect of the pseudocompressibility diminishes, resulting in an incompressible solution.

Computational Method

The numerical algorithm used to integrate Eq. (1) is briefly described. A flux-difference splitting based on Roe's approximate Riemann solver[14] is chosen to upwind-difference the inviscid fluxes $\boldsymbol{E}$, $\boldsymbol{F}$, and $\boldsymbol{G}$. This splitting technique is used separately in each spatial dimension. For three-dimensional conservation equations, the overall discretization is obtained via adding up all three independent discretizations of the flux vectors in each dimension.

The simple flux-difference splitting method gives first-order-accurate spatial differencing. The first-order scheme is a total variation diminishing (TVD)[15] scheme, and its solution is contaminated with a considerable amount of numerical dissipation.[10] The spatial differencing is enhanced to second-order

accuracy by incorporating a discretization similar to a high-resolution TVD scheme.[10-13] The high-resolution TVD schemes are essentially nonlinear schemes. The schemes switch between several difference stencils, such that the schemes adapt to the local solutions in order to give high resolution in regions of smooth solutions while still suppressing spurious oscillations in regions of high-flow gradients (e.g., contact discontinuities). Adapting to the local flux limiters, the local spatial differences can be upwind differences of first-order accuracy or central, one-sided, or upwind-biased differences of second-order accuracy.

The solutions to Eq. (1) are advanced in pseudotime, using linearized Euler-implicit time differencing and local time stepping. An implicit scheme is chosen to avoid a restrictive time-step size when highly refined grids are used to resolve viscous effects. Casting the equations in delta form yields steady-state solutions that are independent of the time-step size. The two-time-level discretization of Eq. (1) can be written as

$$N\Delta Q_n + RES(Q^n) = 0 \tag{2}$$

where $\Delta Q^n = Q^{n+1} - Q^n$. The operator RES gives the residual at time level n and represents the discretized spatial-derivative terms of Eq. (1). The viscous fluxes are centrally differenced in the usual manner and the inviscid fluxes are discretized by applying the high-resolution TVD-like scheme discussed in the last paragraph. The resulting spatial differencing is up to second-order accurate. A hybrid approach[10-13] for the formulation of the operator N is chosen. It uses approximate factorization in crossplanes ($\xi-\eta$ planes) in combination with a symmetric, planar Gauss-Seidel relaxation in the ζ direction. The hybrid scheme with block-tridiagonal implicit factors is written as

$$\begin{aligned}&\left\{M + [B^+ + S^*]_{j-\frac{1}{2}}\Delta_{j-\frac{1}{2}} - [B^- + S^*]_{j+\frac{1}{2}}\Delta_{j+\frac{1}{2}}\right\}^n \\ &\quad \times [M^{-1}]^n \times \left\{M + [C^+ + T^*]_{k-\frac{1}{2}}\Delta_{k-\frac{1}{2}}\right. \\ &\quad \left. - [C^- + T^*]_{k+\frac{1}{2}}\Delta_{k+\frac{1}{2}}\right\}^n \times \Delta Q^n \end{aligned} \tag{3}$$

with

$$M = I/\Delta t J + [A^+ + R^*]_{i-1/2} + [A^- + R^*]_{i+1/2}$$

where I is the identity matrix; where $A^{\pm}$, $B^{\pm}$, and $C^{\pm}$ are the Jacobian matrics of $E^{\pm}$, $F^{\pm}$, and $G^{\pm}$ constructed through the eivengalue decompositions; and where R^*, S^*, and T^* are the linearized coefficient matrices associated with viscous shear fluxes E_V, F_V, and G_V, respectively. The nonlinear updating of the residual during back and forth sweeps in the ζ direction is indicated by $RES(Q^n, Q^{n+1})$ in Eq. (3).

On the computational boundaries, unknown values of Q^n are updated explicitly and ΔQ^n are set to zero. On the wing surface, the no-slip condition is imposed and the normal gradient of the pressure is assumed to vanish. Freestream conditions are specified along the outer boundaries except for the outflow boundary, where the values are computed using extrapolation. Reflection conditions are applied on the plane of symmetry. The flowfield values along the branch cut in the wake are computed by averaging the extrapolates of the dependent variables from above and below. The initial conditions consist of freestream values. The values of TVD limiters along all computational boundaries are set to zero.

Grid Generation

In the generation of a computational grid, a body-conforming grid is desired to simplify the application of boundary conditions and to help maintain the well-orderliness that is useful for vector processing and for various implicit methods with approximate factorization techniques. In addition, the grid points must be concentrated in flowfield action regions to resolve the flow structures. For the vortical flow around the double-delta wing at high angles of attack, these regions are near the apex, kink, leading and trailing edges, wing surface, and in the neighborhood of the leeward vortical cores. To minimize the truncation errors in the Navier-Stokes calculations, the clustered grid is also required to be smoothly varying. Since smoothness is inherent in an elliptic grid, the body-conforming, curvilinear grids used for finite-difference calculations are generated solving a set of Poisson equations.

Two elliptic grids are generated for the test-wing geometry.[1] These grids are of single-block C-H topology. Each grid extends one root chord upstream and downstream of the wing and approximately two chords radially away from the longitudinal axis of the wing. Bilateral symmetry is imposed to reduce the computational domain. Both three-dimensional grids are composed of 53 successive crossplanes which are perpendicular to the longitudinal axis. These crossplanes are clustered near the apex, kink, and trailing edge; the minimum

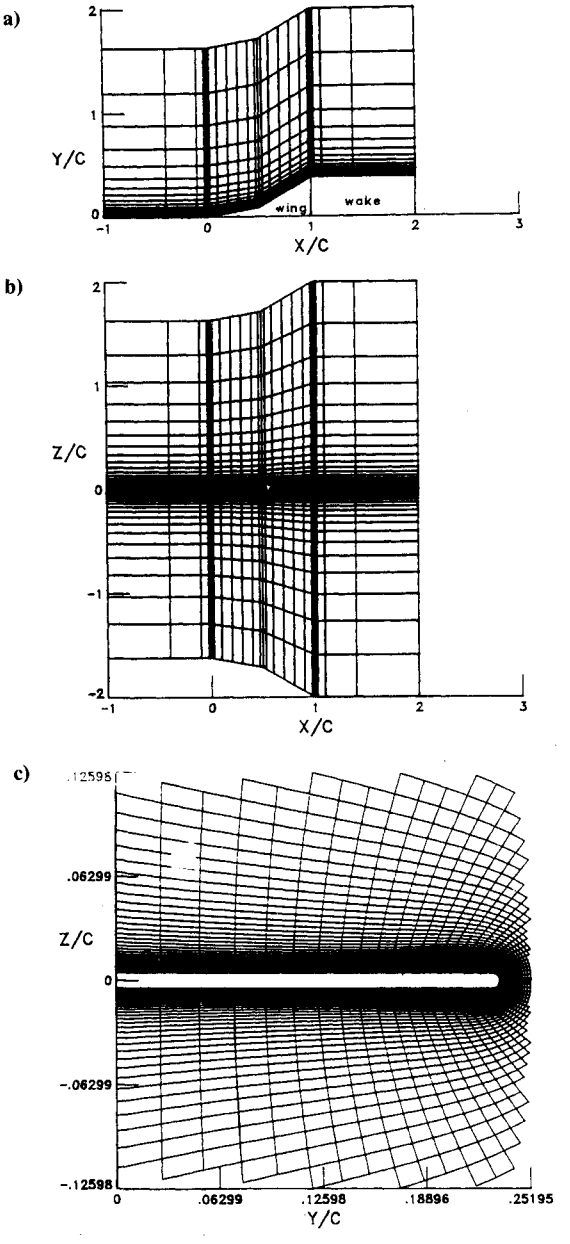

Fig. 3 Three dimensional elliptic grid: a) planform mesh, b) mesh at plane of symmetry, c) crossplane mesh at $X/C = 0.75$.

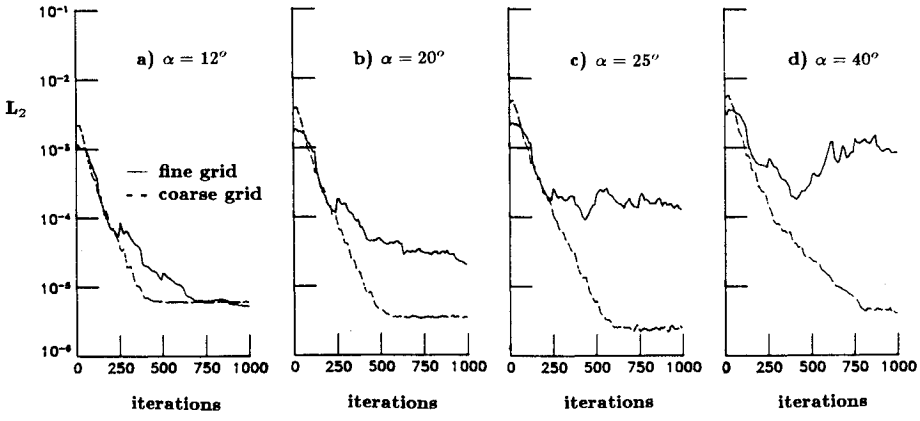

Fig. 4 Convergence rate of L_2 norms.

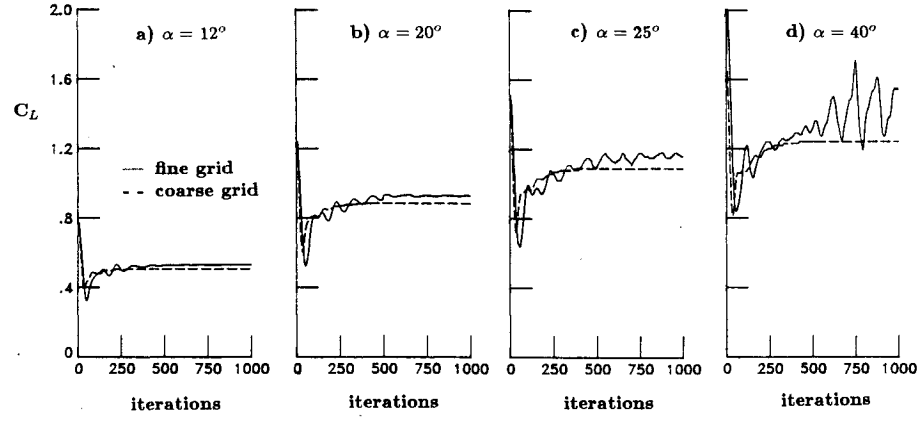

Fig. 5 Convergence history of lift coefficients.

spacing between crossplanes is 3×10^{-3} C. In each crossplane, a nearly-orthogonal mesh is generated between two control lines. The inner line depicts the wing contour and the outer line is a semicircle. Mesh points are clustered near the wing surface and around the leading edge. The directions and spacing of mesh lines are both controlled by proper choice of the source terms in the Poisson equations. In each crossplane, the coarse (fine) mesh has 65 (97) and 65 (167) mesh points in the radial and circumferential directions, respectively. The minimum spacing normal to the wing surface at the trailing edge for the coarse (fine) mesh is 1.7×10^{-4} C (7.7×10^{-5} C). For the sake of clarity, only the coarse grid is shown in Fig. 3.

Navier-Stokes Computations

The flowfield about a round-edged double-delta wing with an aspect ratio of 2.05 is studied here. All edges of the wing are rounded with radii of one half the wing thickness. This geometry was tested by Brennenstuhl and Hummel[1] in a low-speed wind tunnel at $Re = 1.3 \times 10^6$ ($M_\infty \approx 0.1$) and in a water tunnel at $Re = 10^4$. Three-component-balance, pressure-distribution, and flowfield measurements, as well as flow visualization at the wing's surface, were recorded.

The finite-difference computations were carried out in 32-bit word arithmetic on the CDC CYBER 205 vector computer at the NASA Langley Research Center. The central processor unit time per grid point per iteration is 52 μs. All steady-state solutions are calculated for $Re = 1.3 \times 10^6$ ($M_\infty = 0.0$), with local time stepping (CFL = 10) up to 1000 iterations. Fig. 4 shows the numerical efficiency of the present scheme with second-order spatial accuracy. For coarse-grid calculations (dotted lines), the L_2 norms of all residuals are reduced by three orders of magnitude within about 350 ~ 800 iterations for $\alpha = 12° \sim 40°$. For fine-grid calculations (solid lines), the L_2 norms are reduced by about two (one) orders of magnitude within 1000 iterations for $\alpha < 20°$ ($\geq 25°$).

The convergence history of lift coefficient C_L is shown in Fig. 5. For coarse-grid computations (dotted lines), asymptotic steady-state values are reached within 500 iterations for all angles of attack ($\alpha = 12° \sim 40°$). For fine-grid computations, asymptotic steady-state values are obtained within 500 (1000) iterations for $\alpha = 12°$ (20°). For $\alpha \geq 25°$, asymptotic steady-state values cannot be reached within 1000 iterations, and the amplitude of the oscillating lift coefficient becomes larger at higher angle of attack.

The present fine-grid computations (Figs. 4d and 5d) show that asymptotic steady-state solutions cannot be obtained at large angles of attack ($\alpha > 30°$), which signals that the flow is unsteady. Similar trends have been shown in Fujii and Shiff's thin-layer compressible Navier-Stokes calculations.[9] To resolve the flow unsteadiness at large angles of attack, a time-accurate computational algorithm with little numerical dissipation must be developed.

Fine-Grid Solutions

According to the experiment,[1] at $\alpha = 12°$ and $Re = 1.3 \times 10^6$, two primary vortices are formed along the strake and wing leading edges. The shear layer that emanates from the strake leading edge rolls up into a near-conical strake vortex, which is similar to the flow above a slender delta wing. Downstream of the kink an additional vortex, the wing

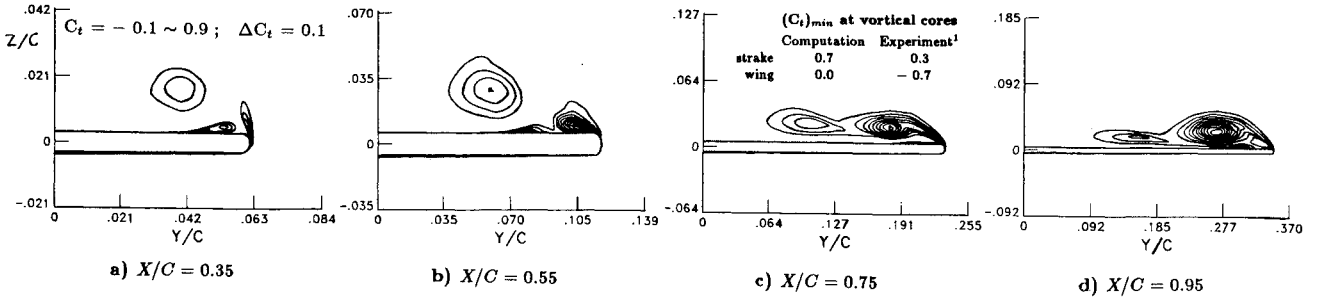

Fig. 6 Total pressure contours at $\alpha = 12°$ (fine grid).

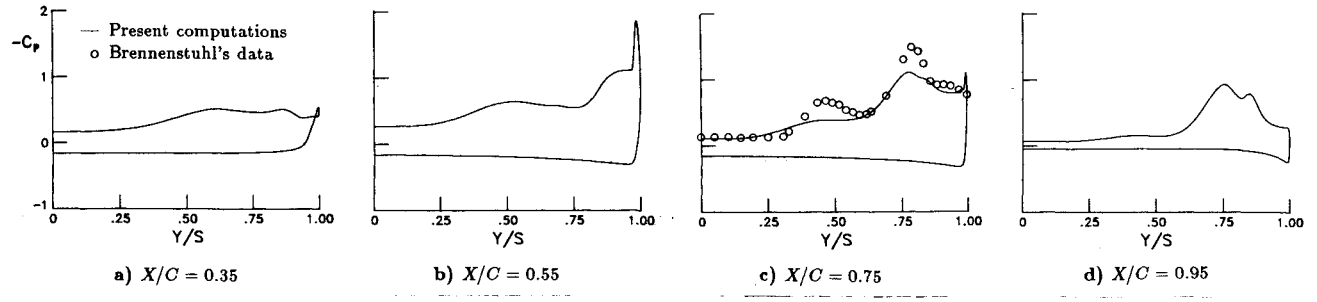

Fig. 7 Spanwise surface pressure coefficients at $\alpha = 12°$ (fine grid).

vortex, is formed above the main wing. The wing vortex is continuously fed with vorticity from the wing leading edge. As a consequence, the vortical strength of the wing vortex increases downstream. At some distance downstream of the kink, the vorticity fed into the strake vortex will gradually diminish. Consequently, the vortical strength of the strake vortex will remain constant or even reduce by viscous dissipation. Further downstream, the two vortices eventually merge into one single vortex.

Computed total pressure contours of fine grid at $X/C = 0.35$, 0.55, 0.75, and 0.95 for $\alpha = 12°$ are shown in Fig. 6. At $X/C = 0.35$, only one primary vortex above the half-wing is visible, which is accompanied by a secondary separation. Upstream of the kink, the crossflow pattern is similar to that at $X/C = 0.35$. Downstream of the kink, at $X/C = 0.55$, the wing vortex is clearly indicated. Further downstream, at $X/C = 0.75$ the weaker strake vortex moves downward and outboard and the stronger wing vortex moves slightly upward and inboard. At $X/C = 0.95$, the two primary vortices are still distinguishable. Although good qualitative agreement with the experimental observations have been obtained, the computed total pressure loss at the strake and wing vortex cores are less than the experimental measurements[1] as compared in Fig. 6c. This points out that greater meshes are required in the neighborhood of vortical cores.

The distributions of spanwise surface static pressure coefficients for $\alpha = 12°$ are plotted in Fig. 7. At $X/C = 0.35$, two suction-pressure peaks of the same magnitude are induced by the strake vortex and its secondary separation. At $X/C = 0.55$, the outer wing vortex induces a much higher suction-pressure peak than that of the inner strake vortex, which is accompanied by a smallest suction-pressure peak due to the secondary separation of the inner strake vortex. At $X/C = 0.75$, the predicted magnitudes of pressure minima due to the primary vortices are lower than the experimental data.[1] Furthermore, the location of secondary separation (Fig. 7c) associated with the primary wing vortex is slightly inboard of that measured in the experiment.[1] This discrepancy is probably caused by the laminar/turbulent transition that was observed in the experiment but is not modeled in the present computations. It might also be attributed to the insufficient crossflow resolution. At $X/C = 0.95$, the suction-pressure level

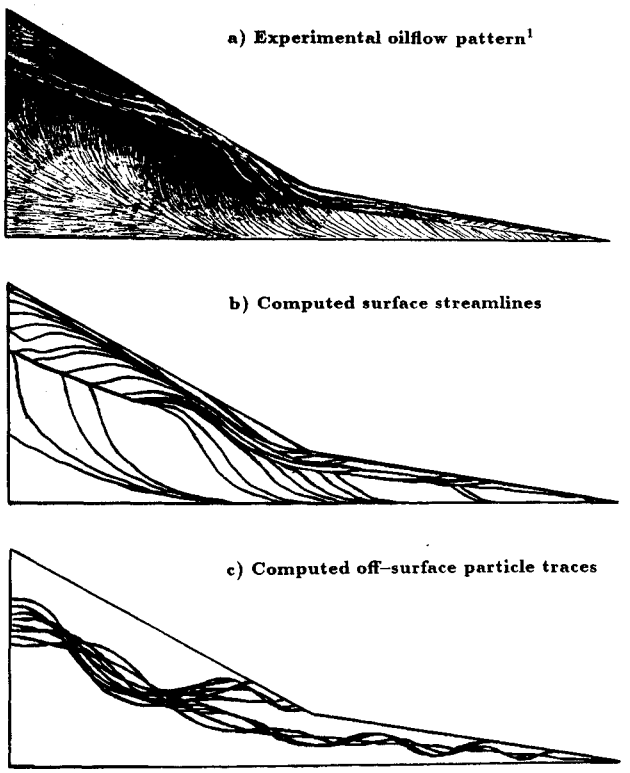

Fig. 8 Comparison of flow patterns at $\alpha = 12°$ (fine grid).

of the relatively much weaker strake vortex is almost flat; the outer wing vortex and its induced secondary separation induce two very high levels of suction-pressure peaks. Therefore, the static pressure distributions (Fig. 7) in a certain degree do reflect the vortical strengths shown in total pressure contours (Fig. 6).

The comparison of flow patterns for $\alpha = 20°$ is shown in Fig. 8. Fig. 8a exhibits the experimental streaklines (white

lines) on a black background. On the main wing, the black region near the leading edge is probably caused by the lack of oil. Fig. 8a indicate that the primary strake and wing vortices can hardly be distinguished on the main wing. The secondary separation line is almost straight on the strake and becomes wavy downstream of the leading-edge kink; it finally straightens and follows the leading-edge slope on the rear part of the wing. The computed surface-flow streamlines (Fig. 8b), black lines on a white background, appear very similar to the experimental streaks. Computed off-surface particle traces (Fig. 8c) clearly show the formation and interaction of the primary strake and wing vortex. The shear layer which emanates from the strake leading edge rolls up into a well-organized vortex. Downstream of the kink, the wing vortex is formed above the main wing. Since these two vortices have the same sense of rotation, they swirl around each other due to mutual induction. Near the trailing edge, the two vortices eventually merge into one single vortex.

Effects of Angle of Attack (Fine Grid)

Figure 9 displays total pressure contours at $X/C = 0.75$ for eight angles of attack. At $\alpha = 6°$, the two primary strake and wing vortices are distinct and separate. From $\alpha = 12°$ to 25°, the vortical strengths become greater and greater (larger total pressure loss); the inner strake vortex moves downward and outboard and the outer wing vortex moves upward and

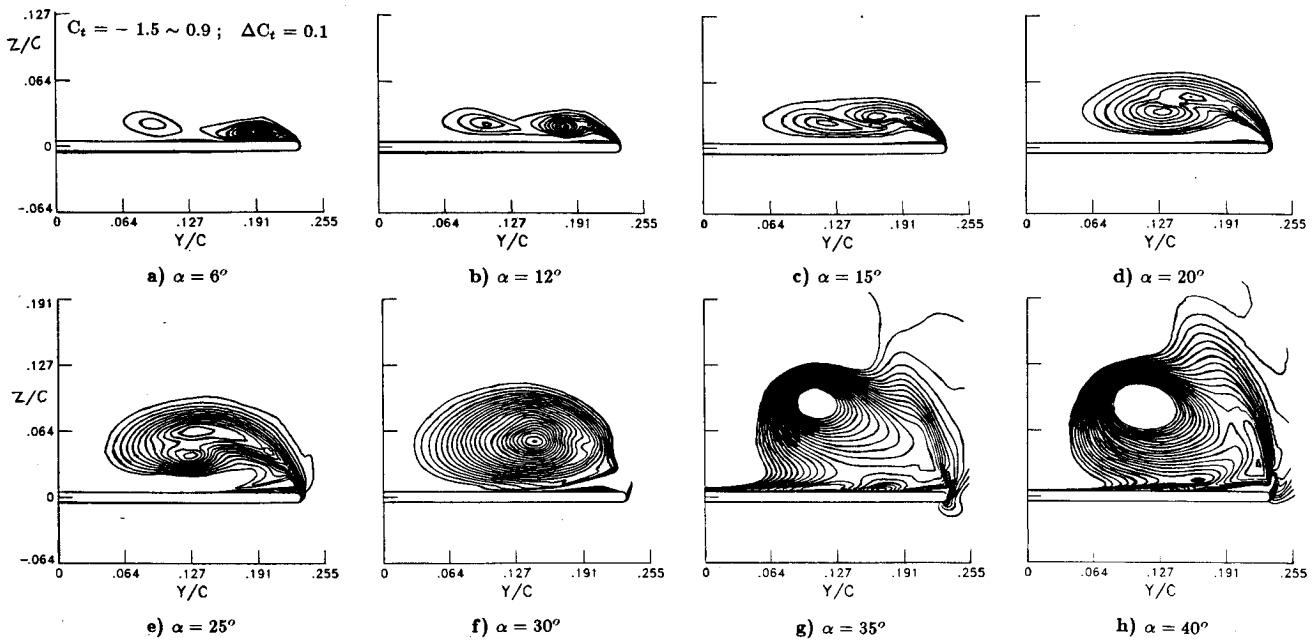

Fig. 9 Total pressure contours at $X/C = 0.75$ (fine grid).

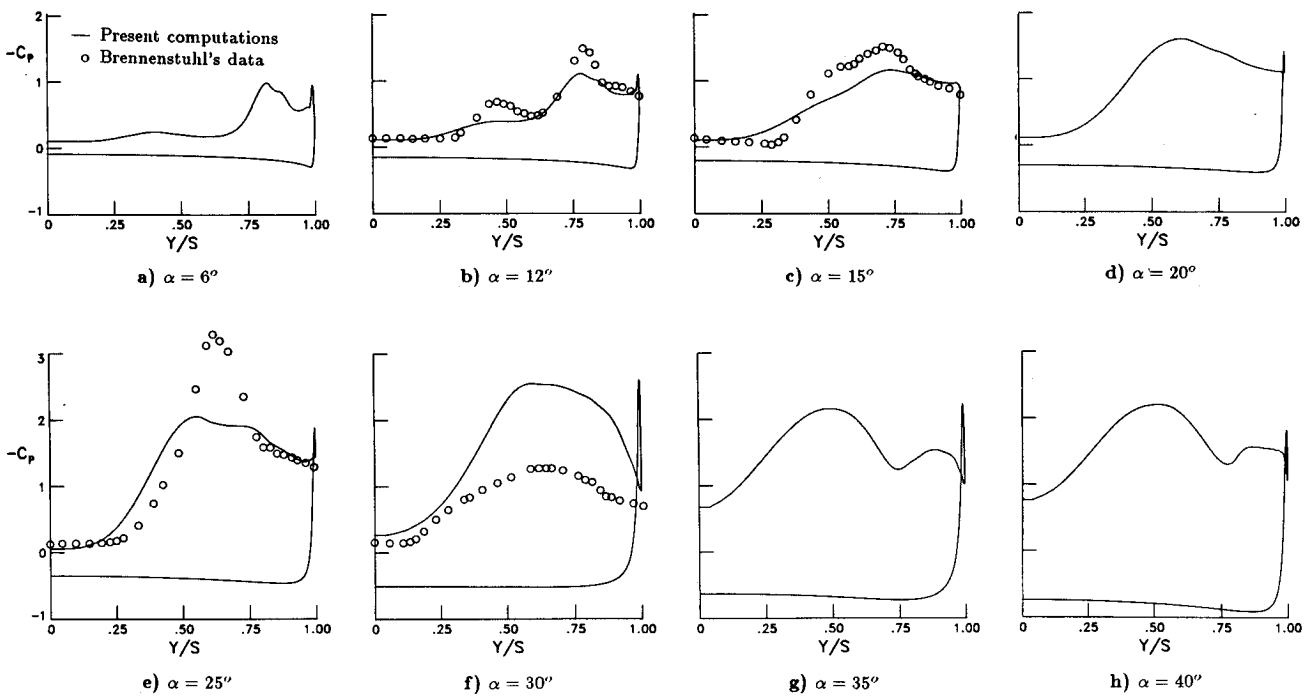

Fig. 10 Spanwise surface pressure coefficients at $X/C = 0.75$ (fine grid).

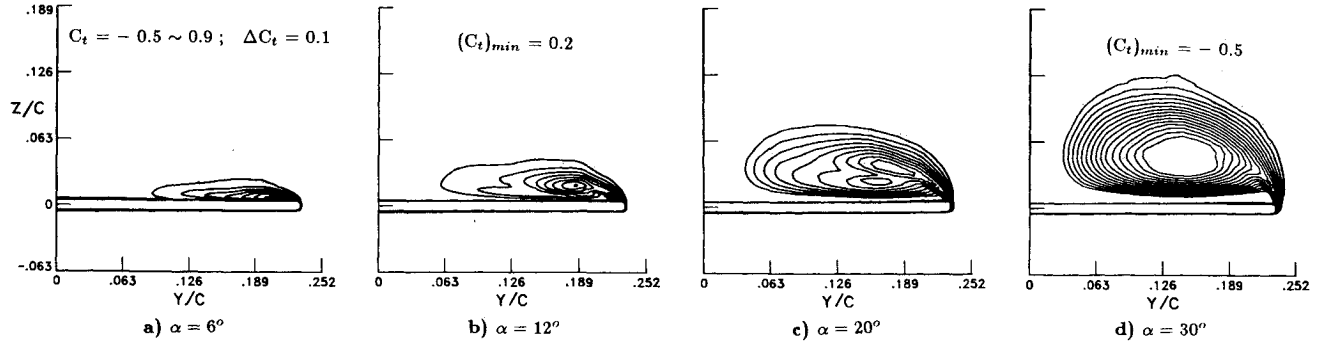

Fig. 11 Total pressure contours at $X/C = 0.75$ (coarse grid).

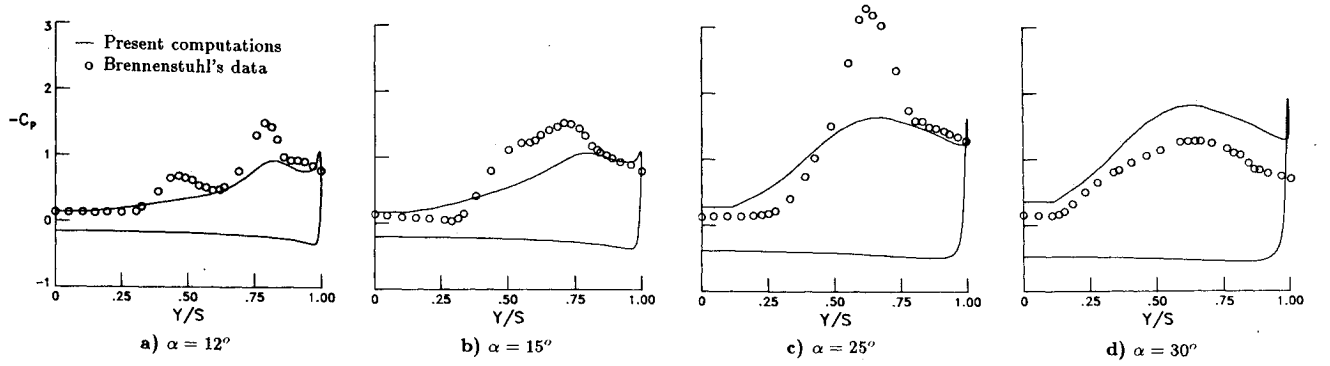

Fig. 12 Spanwise surface pressure coefficients at $X/C = 0.75$ (coarse grid).

inboard. The complete merging takes place at $\alpha = 30°$, i.e., only a single vortex exists. The vortical core swells at $\alpha = 35°$ and further expands at $\alpha = 40°$.

It is observed in water-tunnel studies[1] that the breakdown location of the merged vortex is about at the trailing edge for $\alpha \approx 25°$. At $\alpha = 30°$, vortex breakdown takes place over the wing at $X/C \approx 0.6$. Up to $\alpha = 40°$, the location of vortex breakdown does not pass the kink station. This implies that a well-organized strake vortex persists over the strake part of the wing. Three-component-balance measurements[1] indicate that the onset of vortex breakdown occurs at $\alpha \approx 26°$. However, the type of vortex breakdown (spiral or bubble type) and the magnitudes of velocity components are not measured.

Numerical results indicate that bubble-type vortex breakdowns are obtained for $\alpha = 35°$ and 40°. Upstream of the breakdown location (axial stagnation point), the vortical flow has a jet-like axial velocity, which starts right downstream of the apex. The core flow accelerates to a maximum axial speed of 2.59 (4.94) V_∞ at $X/C = 0.25$ (0.40) for $\alpha = 35°$ (40°). The zone of reversed axial flow (negative-u region) extends from $X/C = 0.95$ to 1.05 (0.85 to 1.03) for $\alpha = 35°$ (40°). The minimum axial velocity component is $-0.15\ V_\infty$ ($-0.15\ V_\infty$) and takes place at $X/C = 1.00$ (0.95) for $\alpha = 35°$ (40°).

The discrepancy in predicting the breakdown location is caused by many factors. Although large-scale vortical structures are successfully simulated, the grid is not fine enough to capture small eddies associated with turbulent flows at very high angles of attack. The laminar/turbulent transition is not modeled in the present numerical schemes and it may not be important in determining the onset of vortex breakdown, but it is expected to be decisive in describing the real flow within and downstream of the breakdown zone. Furthermore, to resolve the flow unsteadiness of breakdown at high Reynolds numbers a time-accurate computational algorithm with little numerical dissipation must be developed. Also, detailed experimental investigations must be carried out to provide more quantitative results for comparisons.

Computed surface static pressure distributions are shown in Fig. 10 and compared with available experimental data[1] for $\alpha = 12°$, 15°, 25°, and 30°. The predicted magnitudes of suction-pressure peaks are smaller than the experimental data for $\alpha = 12°$, 15°, and 25°. On the contrary, the magnitude is larger than the experimental data for $\alpha = 30°$. In general, computed spanwise surface static pressure distributions show good agreements with the experimental data for $\alpha < 25°$.

Coarse-Grid Results

Figure 11 displays the total pressure contours computed with the coarse grid at $X/C = 0.75$ for four angles of attack. At $\alpha = 6°$ or 12°, only a single vortex is clearly visible; on the other hand, two primary vortices are shown in the corresponding fine-grid contours (Fig. 9). At $\alpha = 20°$, it seems that the strake and wing vortices almost complete the merging process. At $\alpha = 30°$, the merged vortex has a relatively diffusive, vortical core. Comparisons of Fig. 9b with 11b and Fig. 9f with 11d indicate that the vortices in coarse-grid computations are too diffusive due to insufficient grid resolution.

Numerical results show a bubble-type breakdown at $\alpha = 40°$. Upstream of the breakdown zone, the core flow accelerates to a maximum axial speed of 1.90 V_∞ at $X/C = 0.45$. The breakdown zone extends from $X/C = 0.65$ to 1.05. The minimum axial velocity component takes place at $X/C = 0.85$, with a value of $-0.29\ V_\infty$. Experimental data of velocity components are needed for meaningful comparisons.

The calculated spanwise surface static pressure distributions are compared with available experimental data for $\alpha = 12°$, 15°, 25°, and 30° in Fig. 12. The comparisons are fairly good. The magnitudes of suction-pressure peaks are all lower than those of fine-grid computations (Fig. 10). Also, the effects of secondary separation on pressure distributions cannot be detected for lack of grid resolution.

Lift Characteristics

Figure 13 displays the lift coefficient vs the angle of attack for the present incompressible Navier-Stokes solutions (lines)

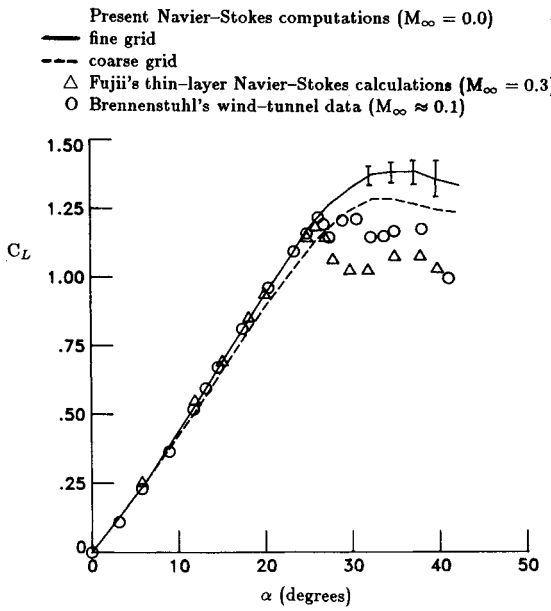

Fig. 13 Lift variation with angle of attack.

and Fujii and Schiff's thin-layer compressible Navier-Stokes calculations (triangles),[9] as well as Brennenstuhl and Hummel's wind-tunnel data (circles).[1] Fumii and Schiff's calculations ($M_\infty = 0.3$) were carried out for a grid of 853,349 points. Their predicted mean lift coefficients compare well with the experimental data up to $\alpha \approx 26°$; at $\alpha > 26°$ the values are underpredicted. The present computations ($M_\infty = 0.0$) show that fine-grid (858,547 grid points) lift coefficients (solid lines) are in good agreement with the experimental data up to $\alpha = 26°$. The mean lift coefficients at $\alpha > 26°$ are overpredicted. The coarse-grid (223,925 grid points) results (dotted lines), which are lower than fine-grid results for all angles of attack, show fairly good agreement with the experimental data. However, none of the fine- and coarse-grid results indicate a sharp decrease in C_L associated with vortex breakdown, as observed in the experimental data.

Conclusions

The numerical simulation of the vortical flow over a round-edged double-delta wing has been studied by solving the incompressible Navier-Stokes equations via an upwind-relaxation finite-difference scheme. From the computed contours of total pressure with the fine grid, it is shown that the main characteristics of the vortex formation and interaction for the strake and wing vortices are well captured at $\alpha \leq 25°$. Also, key features of bubble-type vortex breakdowns at $\alpha = 35°$ and 40° are simulated. Computed spanwise surface static pressure distributions and lift coefficients are in good agreement with the experimental data up to $\alpha = 25°$. On the other hand, although coarse-grid results are fairly good for estimating lift coefficients and spanwise surface static pressure distributions, they cannot predict the detailed structures of the vortical flowfields for lack of grid resolution. Time-accurate computations with a finer grid resolution in the neighborhood of vortical cores are required to investigate the more complicated flow of vortex breakdown.

Acknowledgment

The work of the first author was supported by the NASA Langley Research Center, Hampton, VA, under Contract NAS1-17919.

References

[1]Brennenstuhl, U. and Hummel, D., "Vortex Formation over Double-Delta Wings," *Proceedings of the 13th Congress of the International Council of the Aeronautical Sciences*, AIAA, New York, 1982, pp. 1133-1146.

[2]Verhaagen, N. G., "An Experimental Investigation of the Vortex Flow over Delta and Double-Delta Wings at Low Speed," AGARD-CP-342, Paper 7, April 1983.

[3]Manor, D. and Wenta, W. H., Jr., "Flow over Double-Delta Wing and Wing Body at High α," *Journal of Aircraft*, Vol. 22, Jan. 1985, pp. 78–82.

[4]Erickson, G. E., "Water Tunnel Flow Visualization: Insight into Complex Three-Dimensional Flowfields," *Journal of Aircraft*, Vol. 17, Sept. 1980, pp. 656–662.

[5]Thompson, D. H., "A Visualization Study of the Vortex Flow around Double-Delta Wings," Aeronautical Research Laboratories, Melbourne, Australia, Aerodynamics Rept. 165, Aug. 1985.

[6]Liu, C. H., Krause, E., and Ting, L., "Vortex-Dominated Flow with Viscous Core Structure," AIAA Paper 85–1556, July 1985.

[7]Newsome, R. W. and Kandil, O. A., "Vortical Flow Aerodynamics—Physical Aspects and Numerical Simulation," AIAA Paper 87–0205, Jan. 1987.

[8]Liu, C. H. and Hsu, C. -H., "Vortex Breakdown Simulation at NASA," *Proceedings of the Second International Colloquium on Vortical Flows*, Baden, Switzerland, 1987, pp. 9-17.

[9]Fujii, K. and Schiff L. B., "Numerical Simulation of Vortical Flows over a Strake-Delta Wing," AIAA Paper 87–1229, June 1987.

[10]Hsu, C.-H., Hartwich, P.-M., and Liu, C. H., "Computation of Vortical Interaction for a Sharp-Edged Double-Delta Wing," *Journal of Aircraft*, Vol. 25, May 1988, pp. 442–447.

[11]Hsu, C.-H., Hartwich, P.-M., and Liu, C. H., "Incompressible Navier-Stokes Computations for a Round-Edged Double-Delta Wing," *Journal of Aircraft*, Vol. 25, Aug. 1988, pp. 675–676.

[12]Hartwich, P.-M. and Hsu, C.-H, "High Resolution Upwind Schemes for the Three-Dimensional, Incompressible Navier-Stokes Equations," *AIAA Journal*, Vol. 26, Nov. 1988, pp. 1321–1328.

[13]Hartwich, P.-M., Hsu, C.-H., and Liu, C. H., "Vectorizable Implicit Algorithms for the Flux-Difference Split, Three-Dimensional Navier-Stokes Equations," *Journal of Fluids Engineering*, Vol. 110, Sept. 1988, pp. 297–305.

[14]Roe, P. L., "Approximate Riemann Solvers, Parameter Vectors, and Difference Schemes," *Journal of Computational Physics*, Vol. 43, Oct. 1981, pp. 357–372.

[15]Harten, A., "High Resolution Schemes for Hyperbolic Conservation Laws," *Journal of Computational Physics*, Vol. 49, March 1983, pp. 357–393.